2-1-2021

Biophysical Characteristics of Lipid-Induced Aβ Oligomers Correlate to Distinctive Phenotypes In Transgenic Mice

Jhinuk Saha
University of Southern Mississippi

Dexter N. Dean
University of Southern Mississippi

Shailendra Dhakal
University of Southern Mississippi

Kelli A. Stockmal
University of Southern Mississippi

Sarah E. Morgan
University of Southern Mississippi

See next page for additional authors

Received: 1 September 2020 | Revised: 3 December 2020 | Accepted: 14 December 2020

DOI: 10.1096/fj.202002025RR

RESEARCH ARTICLE

THE FASEB JOURNAL

Biophysical characteristics of lipid-induced Aβ oligomers correlate to distinctive phenotypes in transgenic mice

Jhinuk Saha[1] | Dexter N. Dean[1] | Shailendra Dhakal[1] | Kelli A. Stockmal[2] | Sarah E. Morgan[2] | Kristy D. Dillon[3] | Munir F. Adamo[3] | Yona Levites[3] | Vijayaraghavan Rangachari[1,4]

[1]Department of Chemistry and Biochemistry, School of Mathematics and Natural Sciences, University of Southern Mississippi, Hattiesburg, MS, USA

[2]School of Polymer Science and Engineering, University of Southern Mississippi, Hattiesburg, MS, USA

[3]Center for Translational Research in Neurodegenerative Disease, University of Florida, Gainesville, FL, USA

[4]Center for Molecular and Cellular Biosciences, University of Southern Mississippi, Hattiesburg, MS, USA

Correspondence
Vijayaraghavan Rangachari, Department of Chemistry and Biochemistry, School of Mathematics and Natural Sciences, University of Southern Mississippi, Hattiesburg, MS, USA.
Email: vijay.rangachari@usm.edu

Present address
Dexter N. Dean, Laboratory of Protein Conformation and Dynamics, Biochemistry and Biophysics Center, National Heart Lung and Blood Institute, National Institutes of Health, Bethesda, MD, USA

Funding information
National Institute of Aging, Grant/Award Number: 1R56AG062292-01; National Institute of General Medical Sciences, Grant/Award Number: R01GM120634; National Science Foundation, Grant/Award Number: NSF CBET 1802793, NSF

Abstract

Alzheimer's disease (AD) is a progressive neurodegenerative disorder that affects cognition and memory. Recent advances have helped identify many clinical sub-types in AD. Mounting evidence point toward structural polymorphism among fibrillar aggregates of amyloid-β (Aβ) to being responsible for the phenotypes and clinical manifestations. In the emerging paradigm of polymorphism and prion-like propagation of aggregates in AD, the role of low molecular weight soluble oligomers, which are long known to be the primary toxic agents, in effecting phenotypes remains inconspicuous. In this study, we present the characterization of three soluble oligomers of Aβ42, namely 14LPOs, 16LPOs, and GM1Os with discreet biophysical and biochemical properties generated using lysophosphatidyl glycerols and GM1 gangliosides. The results indicate that the oligomers share some biophysical similarities but display distinctive differences with GM1Os. Unlike the other two, GM1Os were observed to be complexed with the lipid upon isolation. It also differs mainly in detection by conformation-sensitive dyes and conformation-specific antibodies, temperature and enzymatic stability, and in the ability to propagate morphologically-distinct fibrils. GM1Os also show distinguishable biochemical behavior with pronounced neuronal toxicity. Furthermore, all the oligomers induce cerebral amyloid angiopathy (CAA) and plaque burden in transgenic AD mice, which seems to be a consistent feature among all lipid-derived oligomers, but 16LPOs and GM1Os displayed significantly higher effect than the others. These results establish a correlation between molecular features of Aβ42 oligomers and their distinguishable effects in transgenic AD mice attuned by lipid characteristics, and therefore help bridge the knowledge gap in understanding how oligomer conformers could elicit AD phenotypes.

Abbreviations: 14LPOs, C14 lysophospholipid-derived oligomers; 16LPOs, C16 lysophospholipid-derived oligomers; Aβ, Amyloid-β; CAA, cerebral amyloid angiopathy; CMC, critical micelle concentration; GM1Os, GM1 ganglioside-derived oligomers; LFAOs, large fatty acid-derived oligomers; LMW, low molecular weight; ThT, thioflavin-T.

Jhinuk Saha and Dexter N. Dean contributed equally to this study.

1445151 and NRT 1449999; National Center for Research Resources, Grant/Award Number: 5P20RR01647-11; National Institute of General Medical Sciences, Grant/Award Number: 8 P20 GM103476-11

KEYWORDS

amyloid-β, Alzheimer disease, cerebral amyloid angiopathy, membrane lipids, oligomers, phenotypes

1 | INTRODUCTION

Alzheimer disease (AD) is a fatal neurodegenerative disorder characterized by a progressive and irreversible cognitive decline and memory loss among the elderly. The AD brain is characterized by two pathological hallmarks; intracellular tangles comprised of hyper-phosphorylated tau protein and extracellular plaques composed of amyloid-β (Aβ) peptide aggregates.[1] However, the levels of low molecular weight (LMW) oligomers of Aβ correlate better with cognitive decline.[2-5] It has now been well established that LMW oligomers are the primary toxic species responsible for early neuronal dysfunction in AD.[6-8] Therefore, understanding how Aβ oligomers are generated and what their structural features are, is of significant interest that may hold the key to the development of therapeutics for AD.

The stochasticity involved in Aβ aggregation, especially during early stages, gives rise to multiple pathways of aggregation and with a diverse range of aggregate sizes and conformations.[9] Because of this, conformational heterogeneity and structural polymorphism are commonly observed among Aβ aggregates.[10-14] Perhaps a profound impact of this is that the aggregate polymorphism may direct correlate to the clinical phenotypes observed among AD patients.[15-18] Aggregates with distinct conformations have been identified among both familial and idiopathic AD brains.[18] Differences in the structure between Aβ fibrils propagated with endogenous seed derived from rapid-onset (rAD) and sporadic AD brains have reinforced the idea that conformational strains are in part responsible for different phenotypes observed.[19] Therefore, understanding the relationship between aggregate conformation and their pathological function, along with the mechanisms underlying strain generation and propagation, has become imperative in deciphering AD pathogenesis.

Aβ aggregation is sensitive to the environmental conditions and interactions with other biomolecules.[20-22] Being a part of the transmembrane domain of the amyloid precursor protein (APP), Aβ is influenced by membrane lipids during the early stages of Aβ aggregation.[23-27] Lipid-associated Aβ has also been observed among AD patients. For instance, a novel membrane-bound Aβ species was isolated from postmortem AD brains that were thought to trigger early stages of disease pathology.[28,29] Aβ was also observed to be tightly bound to GM1 gangliosides, one of the most abundant gangliosides in the brain and constitutes a prime component of lipid rafts.[30] It was later determined that GM1 binds Aβ with micromolar (μM) affinity[31,32] and induces a β-sheet secondary structure transition.[33-36] Aβ also binds and undergoes a structural transition to β-sheet in the presence of negatively charged lipid bilayer vesicles (liposomes).[37-39] Similarly, micelles made up of spherical monolayers have also been shown to stimulate Aβ aggregate formation.[40,41] Work from our lab has shown that distinct oligomers of Aβ are generated in the presence of anionic micelles composed of fatty acids. These oligomers, termed large-fatty acid-derived oligomers (LFAOs) show many interesting biophysical and biochemical properties.[9,22,42-45] LFAOs undergo faithful propagation to fibrils containing repeating oligomer assemblies in vitro,[9] and a bilateral injection of these oligomers into neonatal CRND8 transgenic AD mice selectively induced Aβ deposition within the cerebral vasculature, leading to a condition known as cerebral amyloid angiopathy (CAA).[45] This led us to hypothesize that the faithful propagation of biophysically distinguishable Aβ oligomers toward structurally distinct fibrils may underpin the mechanisms governing clinical manifestations in AD. In this report, we sought to investigate the effect of micelle-forming anionic phospholipids on the biophyscial and biochemical characteristics of oligomers specifically using two anionic lysophosphatidyl glycerols (LPGs) with varying acyl chain lengths and a neutral sphingolipid, GM1 ganglioside. LPGs are good models of micellar phospholipids, while GM1 gangliosides are a major component of membrane lipids and lipid rafts. We show that the LPG-derived oligomers, 14LPOs and 16LPOs, share many biophysical properties with LFAOs, while GM1-derived oligomers, GM1Os show some commonality but are more biophysically distinctive than the other oligomers. They also induce higher degrees of cytotoxicity and exacerbation of amyloid pathology in CRND8 mice brains. In addition, GM1Os and 16LPOs also induce highest level of CAA phenotype among the oligomers. These results bring to light how the physiochemical nature of micellar lipids can be tuned to induce biophysically distinguishable oligomers and how such properties correlate with their effect in mice brains. These results also refocus our attention toward unifying and differential characteristics of lipid-derived oligomers to potentiate as "strains" in inducing specific phenotypes in AD.

2 | MATERIALS AND METHODS

2.1 | Materials

Lyophilized stocks of synthetic Aβ42 WT were purchased from the Yale School of Medicine (New Haven,

CT) and from Dr Chakraborty's lab at the University of Mississippi. The monoclonal antibody Ab5 was obtained from Levites lab at the University of Florida (Gainesville, FL). Size exclusion chromatography (SEC) columns (Superdex-75 HR 10/30) were purchased from GE Life Sciences (Marlborough, MA). LPG (C14:0 and C16:0) and GM1 lipids were purchased from Avanti Polar Lipids, Inc (Alabaster, AL) while C12:0 NEFA was purchased from NuCheck Prep, Inc (Elysian, MN). Tris base, Tris hydrochloride, and sodium dodecyl sulfate (SDS) were purchased from Sigma-Aldrich (St. Louis, MO). Other routinely used chemicals, reagents, and consumables were purchased from either VWR, Inc (Radnor, PA) or Thermo Fisher Scientific, Inc (Waltham, MA).

2.2 | Purification of Aβ monomers

Synthetic Aβ (0.5-2 mg of lyophilized peptide) was dissolved in 490 μL of nanopure H_2O (npH_2O) and allowed to stand at 25°C for 0.5-1 hours. Ten minutes before loading onto a Superdex-75 HR 10/30 SEC column attached either to an AKTA FPLC system (GE Healthcare, Buckinghamshire) or a BioLogic DuoFlowTM system (Bio-Rad), NaOH was added to a final concentration of 10 mM. Monomer was then purified by loading the sample onto a pre-equilibrated (20 mM Tris, pH 8.0) column and fractionating at a flow rate of 0.5 mL/min at 25°C. Fractions of 500 μL were collected, and monomeric Aβ was found to elute in between 23 and 27 fractions. Cary 50 UV–vis spectrometer (Agilent Technologies, Inc; Santa Clara, CA) was used to determine the molar concentration of Aβ in each fraction using Beer-Lambert's law ($\varepsilon = 1450\ cm^{-1}\ M^{-1}$ at 276 nm corresponding to the single tyrosine residue). Matrix-assisted laser desorption/ionization time-of-flight mass spectrometry (MALDI-Tof) was used to confirm the purity and integrity of the peptide. The purified monomers were stored at 4°C in siliconized Eppendorf tubes to minimize protein retention on the tubes and used to initiate experiments within 48 hours of purification.

2.3 | Purification of Aβ oligomers

Purification of Aβ oligomers was initiated by incubating freshly purified Aβ monomer (50 μM) with the specified lipid species in the conditions listed below. LFAOs, 5 mM C12:0 NEFA; 14LPO, 0.4 mM C14:0 LPG; 16 LPO, 0.15 mM C16:0 LPG; GM1O, 75 μM GM1. Additionally, 50 mM NaCl and 0.01% NaN3 were added to all reactions prior to incubation at 37°C in quiescent conditions for 48 hours. The samples were then purified via SEC, as described above, after first pelleting the insoluble peptide by centrifugation at 18 000*g* for 20 minutes. Fractions of 500 μL were collected, and Aβ oligomers were fractionated in the 18-20 fractions. The molar concentration was determined by UV–vis spectroscopy, as described above. Samples were either stored at 4°C in siliconized Eppendorf tubes and used for experimentation within 72 hours or lyophilized and kept at −80°C for extended storage prior to experimentation.

2.4 | Lyophilization and resuspension of Aβ

For lyophilization, aliquots of either 1 or 5 μg were made and flash-frozen by plunging into liquid N2 for 30 seconds prior to freeze-drying overnight using a FreeZone TriadTM freeze dry system (Labconco Corp.; Kansas City, MO) maintained at 0.420 mBar. Lyophilized samples were then stored at −80°C until use. To resuspend the lyophilized samples for experimentation, either nanopure H_2O or Tris buffer (pH 8.0) was added to reach the desired molar concentration of peptide, and the sample was allowed to stand at 4°C for at least 1 hour prior to centrifugation at 18 000 *g* for 20 minutes. The supernatant was then carefully removed and used for experiments.

2.5 | Generation of Aβ fibrils

Aβ monomer (100-150 μM) was added to 150 mM NaCl and allowed to incubate at 37°C in quiescent conditions for 4-5 days for Fon generation. After incubation, the sample was subjected to centrifugation at 18 000 *g* for 20 minutes before carefully discarding the supernatant and resuspending the pellet in fresh 20 mM Tris (pH 8.0) with 0.01% NaN3. ThT fluorescence and centrifugation were used to determine percentage conversion to Aβ fibrils, which was typically 80%-90%. Fibrils were stored at 4°C and used within 30 days.

2.6 | Oligomer seeding reactions

Aβ monomer (25 μM) was seeded with 5 μM oligomer seeds in 20 mM Tris (pH 8.0) with 50 mM NaCl and 50 μM ThT. The reactions were kept in BioTek Synergy 96 well plate reader at 37°C and ThT fluorescence was monitored up to 48 hours. All experiments were carried out by adding 200 μL of the reaction mixture in Corning 96-well plate (black). ThT fluorescence was recorded after an interval of every 10 minutes using excitation at 452 nm and emission at 485 nm at 37°C, shaking samples for 1 second before each read. The kinetics data were processed by subtracting the blank buffer reading from the experimental data followed by normalization using the OriginLab 8.0 program.

2.7 | Partially denaturing and PAGE with immunoblotting

Samples were diluted into 1× Laemmli loading buffer with 1% SDS and loaded without boiling, onto either 4%-12% NuPAGE or 4%-20% Bis-Tris Bio-Rad TGX gels. Pre-stained molecular-weight markers (Novex Sharp Protein Standard, Life Technologies) were run in parallel for MW determination in denaturing PAGE. For immunoblotting, proteins were transferred onto a 0.2 μm nitrocellulose membrane (Bio-Rad). Following the transfer, the immunoblot was boiled for 1 minutes in a microwave oven in 1× PBS, followed by blocking for 1.5 hours at 25°C in 1× PBS containing 5% nonfat dry milk with 1% Tween 20. Blots were then probed overnight at 4°C with a 1:6000 dilution of Ab5 monoclonal antibody, whose epitope is 1-16 sequence of Aβ. Following primary incubation, blots were probed with a 1:6000 dilution of anti-mouse, horseradish peroxidase-conjugated secondary antibody for 1.5 hours at 25°C before being imaged using a Super SignalTM West Pico Chemiluminescent Substrate kit (Thermo Fisher Scientific). Dot blots. Samples (225 ng in 5 μL) were spotted onto a 0.2 μm nitrocellulose membrane and allowed to dry at room temperature for 1 hour. The blots were blocked for 1.5 hours with 1× PBS containing 5% nonfat dry milk and probed overnight at 4°C with 1 : 2000 and 1:6000 dilutions of polyclonal conformational specific antibody OC (Millipore Inc) and A11, respectively, along with Ab5 monoclonal antibody. Blots were then incubated with anti-rabbit (for OC and A11) or anti-mouse (for OC) horseradish peroxide (HRP) conjugated secondary antibody for 1.5 hours and developed with ECL reagent (Thermo Scientific).

2.8 | Curcumin and ANS fluorescence

Curcumin, and 8-anilino-napthalene-1-sulfonic acid (ANS) fluorescence were measured on a Cary Eclipse AQ6fluorometer (Agilent Technologies, Inc) in scan mode. Fluorescence spectra for curcumin were obtained by exciting the sample at 430 nm, while scanning emission between 470 and 600 nm upon the addition of buffered Aβ samples (5-7 μM) and curcumin (5 μM) in 25% EtOH. The slit widths for excitation and emission were kept constant at 10 nm. The data were normalized against the concentrations of the oligomers and averaged for three independent data sets. For ANS, Aβ samples (3 μM) were equilibrated for 2 minutes with ANS (100 μM) in 20 mM Tris pH 8.00 before measuring the fluorescence using excitation at 388 nm and scanning emission between 400 and 650 nm. The integrated intensity was plotted against the wavelength for each sample was plotted as bar-graphs and averaged for three independent data sets.

2.9 | Fourier transform infrared (FTIR) spectroscopy

Lyophilized Aβ samples were resuspended in D_2O to a final concentration of 1 mM before accumulating spectra on a Nicolet 6700 instrument equipped with an ATR accessory. A total of 64 accumulations were collected by scanning 4000-650 cm^{-1} at a resolution of 4 cm^{-1}. Spectra were processed by blank subtraction (using D_2O as the blank) and baseline correction using the OriginLab 8.0 program.

2.10 | Circular dichroism (CD) spectroscopy and thermal denaturation

Far UV CD spectra (260-190 nm) for the oligomers (5-8 μM) were collected on a Jasco (Easton, MD) J-815 spectropolarimeter using a 1 mm pathlength cuvette with an average of 6-16 spectral scans at a rate of 50 nm/min (8 seconds response time, 1 nm bandwidth, 0.1 nm data pitch). Averaged spectra were smoothed using the Savitzky-Golay algorithm with a convolution width of 15 using the Jasco spectrum analysis program. Temperature stability analysis was performed using SDS as a denaturant as described prior.[46] Briefly, SDS (1% wt/vol) was added to a solution of Aβ oligomers (1 μM) in a 1 cm pathlength cuvette, followed by heating from 10 to 90°C, while monitoring the signal at 208 nm that corresponds to the emergence of an α-helical structure. In addition, the far-UV scans of pre- and post-melt samples were measured. The data were processed by normalizing from 0 to 1, where 1 and 0 represent the fully melted and unmelted oligomers, respectively. The normalized values of fully melted samples were calculated by correlating the 90°C data with the post-melt scans wherein the maximum difference in ellipticity between 222 and 208 nm to be <0.1 was considered to be 100% helix based on established observations on SDS-protein systems.[47-49] The data obtained was fit using the Boltzman function in OriginLab 8.0 program to derive T_m values.

Thermodynamic deconvolution of the data was performed as follows: The equilibrium constant K at a given temperature is expressed as:

$$K = \frac{[N]}{[D]}$$

where N and D represent native and denatured oligomers, respectively. The change in.

The fraction denatured, α is expressed as:

$$\alpha = \frac{[D]}{[D] + [N]} = \frac{[\theta] - [\theta]_N}{[\theta]_D - [\theta]_N}$$

where θ is the ellipticity at λ_{208} and K is expressed as,

$$K = \frac{\alpha}{1-\alpha}$$

As we know,

$$\Delta G = -RT \ln K = \Delta H - T\Delta S$$

From this, we can deduce,

$$\ln\left(\frac{\alpha}{1-\alpha}\right) = -\frac{\Delta H}{RT} + \frac{\Delta S}{R}$$

From this equation, linear vant Hoff's plots were generated from which ΔH and ΔS were calculated from the slope and y-intercept, respectively.

2.11 | Dynamic light scattering (DLS)

DLS was collected by averaging 12 runs of 10 seconds each with a pre-equilibration time of 30 seconds using a Zetasizer Nano S instrument (Malvern, Inc, Worcestershire, UK) with 70 µL volume and 1 cm cuvette pathlength. The diameter was determined using the volume (%) function.

2.12 | Electrospray ionization mass spectrometry (ESI-MS)

All samples were evaporated to dryness using vacuum evaporation followed by resuspension at a concentration of 10 µM in a H_2O:CH_3CN:HCOOH (1:1:0.2) solvent. Samples were analyzed by direct infusion into a FinniganTM LXQTM ion trap mass spectrometer (Thermo Fisher Scientific) operated in negative ion mode. Signals were accumulated by scanning the spectrum from 150 to 2000 m/z for a total of 3 minutes (~800 total scans) at a constant flow rate of 100 µL/min. Other instrument parameters were kept as follows: spray voltage (5 kV), capillary temperature (275°C), capillary voltage (−42 V), and automatic gain control (1.5 × 104).

2.13 | Analytical ultracentrifugation

Sample Preparation A 4 mM stock solution of HiLyte 647 in 50% DMSO was diluted to 160 µM aliquot, which was incubated with 10 µM isolated oligomer (14LPO, 16LPO, LFAO & GM1O) in 10 mM sodium phosphate buffer at pH 8, and was incubated overnight at 4°C kept with constant orbital shaking at 80 rpm. The free dye was removed from the dye-protein mixture using 7 kDa Zeba Spin desalting columns in 10 mM sodium phosphate buffer at pH 8 (Thermo Scientific) by centrifuging samples at 900 *g* at 4°C for 1 minutes. The dye and protein absorbance were measured using a Cary 50 UV–vis spectrometer (Agilent Technologies, Inc; Santa Clara, CA) to determine the amount of dye bound to protein. Sedimentation velocity experiments were performed in a Beckman XL-I centrifuge (Beckman Coulter, Inc, Indianapolis, IN) using absorbance and interference optics by measuring intensity scans at 280 nm at the Physical Biochemistry Facility at Florida State University. The experiments were performed at 20°C in two-channel Epon centerpieces with an AN60 Ti rotor at 55, 000 rpm. A 10 mM sodium phosphate at pH 8.0 buffer was the used for protein solubilization. Data were processed and analyzed using the SedFit program[50] to generate c(S) and MW distributions. The frictional coefficient (f/f0) value of 1.4 was used for data processing and calculations. The partial specific volume at 20°C of the protein (0.7021 $cm^3\ g^{-1}$) was used that was estimated from the peptide sequence.

2.14 | Proteinase K (PK) digestion

A 20 mg/mL of PK stock solution from Ambion was diluted to 57 ng/mL in 20 mM Tris pH 8.0 to digest 451.5 ng of each oligomer sample (16LPO, 14LPO, GM1O, and LFAO) by shaking at 200 rpm at 37°C for 40, 30, 20, and 10 minutes, respectively. The reactions were quenched with 0.5 mM PMSF for 1 minute. Subsequently, ~337 ng of protein for each oligomer sample was run on 1% SDS PAGE gel and we transferred onto a 0.2 µm nitrocellulose membrane (Bio-Rad) for immunoblotting. Immunoblots were probed with a 1:6000 dilution of Ab5 monoclonal antibody & anti-mouse, horseradish peroxidase-conjugated secondary antibody, respectively. The immunoblots were imaged using a Super Signal West Pico Chemiluminescent Substrate kit (Thermo Fisher Scientific). Oligomer band intensities in the gel were calculated by choosing a 6 mm^2 area between molecular weight 50-80 kDa and subtracting the intensity of blank on a similar area of the gel with the help of Image Lab (Bio-Rad) software. Intensity vs time plots were then plotted using OriginLab 8.0.

2.15 | Atomic force microscopy

Peptide oligomer and fibril samples were prepared following our previously published procedure.[46] An acidic solution of 3-aminopropyltriethoxysilane (500 µL of APTES in 50 mL of 1 mM acetic acid) was prepared and 150 µL was deposited onto freshly cleaved mica. After 20 minutes, the solution was decanted from the surface and the substrate was washed three times with 150 µL of nanopure DI H_2O. The substrates were

then dried with a stream of N2 and set in a desiccator for an hour. AFM samples were then prepared by depositing 150 μL of oligomer or fibril solution (2 μM in 20 mM Tris-HCl, pH 8.0). After 30 minutes, the solution was decanted and the substrates were dried under a stream of N2. AFM samples were stored in the desiccator until imaging. Image analysis was conducted using a Dimension Icon Atomic Force Microscope (Bruker) in PeakForce Tapping mode equipped with an SNL-C cantilever (nom. tip radius of 2 nm; nom. resonance frequency of 56 kHz; nom. spring constant of 0.24 N/m) in a standard probe holder under ambient conditions. Images were acquired with 512 × 512 data point resolution in NanoScope v8.15 software and analyzed in NanoScope Analysis v1.50.

2.16 | NMR

The ^{1}H NMR spectra were acquired on the Bruker Advance—III-HD 850 MHz NMR spectrometer equipped with a Bruker TCI cryoprobe at the high field NMR facility of the University of Alabama, Birmingham. The spectra of the samples (10-12 μM) in 10 mM phosphate buffer at pH 8.0 with 10% D_2O were collected at 25°C with 6144 or 8192 scans with 14 ppm sweep width centered around water peak with a D1 delay of 1.0 second. Excitation-sculpting water suppression (zgesgp) was used. The data were processed using Bruker TopSpin 3.5 analysis software with standard methods with phase corrections.

2.17 | Cell viability XTT assay

SH-SY5Y human neuroblastoma cells (ATCC, Manassas, VA) were plated in a clear 96 well-plate at a density of approximately 20 000 cells/well in growth media containing 1:1 mixture of DMEM/F12 medium with 10% fetal bovine serum and 1% Pen-Strep at 37°C in a humidified atmosphere of 5.5% CO2. After 24 hours, media was replaced with freshly prepared Aβ oligomers in siliconized tubes resuspended in growth media and incubated for 40 hours. Cell viability assay was performed using 2,3-bis(2-methoxy-4-nitro-5-sulfophenyl)-5-[(phenylamino)carbonyl] -2H- tetrazolium hydroxide (XTT) cell viability assay kit (Biotium). Absorbance was measured at 475 and 660 nm using Synergy HTX Multi-Mode Reader- BioTek Instruments.

2.18 | Tg CRND8 mice injections and immunohistochemistry

2.18.1 | Mice

All animal husbandry procedures performed were approved by the Institutional Animal Care and Use Committee. TgCRND8 were maintained as described before,[51] transgenic males were crossed with B6C3F1 ntg females.

2.18.2 | Neonatal injections

TgCRND8 mice were injected with 2 μL of 10 μM isolated oligomers (14LPOs, 16LPOs, LFAOs, and GM1Os) in 10 mM sodium phosphate buffer at pH 8.00, ICV into both hemispheres using a 10 mL Hamilton syringe with a 30 g needle on day P0 as described before[46,52] and aged till 2 months. Aβ levels from the Ripa, 2% SDS, and 70% FA-extracted samples were quantified using end-specific sandwich ELISA as previously described.[53] Aβ40 was captured with mAb 13.1.1 (human Aβ35-40 specific; TE Golde) and detected by HRP-conjugated mAb 33.1.1 (human Aβ1-16; TE Golde). Aβ42 was captured with mAb 2.1.3 (human Aβ35-42 specific; TE Golde) and detected by HRP-conjugated mAb 33.1.1 (human Aβ1-16; TE Golde). ELISA results were analyzed using SoftMax Pro software.

2.18.3 | Immunohistochemical imaging and image processing

Right hemibrain was fixed in 4% paraformaldehyde. Immunohistochemical staining was performed by biotinylated pan Aβ pan antibody mAb5 (1:1500, T. Golde). To detect we used biotinylated secondary antibody and ABC-horseradish peroxidase staining kits (Vector Laboratories, Burlingame, CA). After development by 3,3′-Diaminobenzidine (DAB) (Sigma-Aldrich) substrate and counterstaining with hematoxylin, the slides were coverslipped and images were scanned by Aperio XT System (Leica Biosystems, Buffalo Gove, IL, USA) and analyzed using either Aperio positive pixel count or ImageJ program. Brightness and contrast alterations were applied identically on captured images using Adobe Photoshop CS3.

2.18.4 | Quantification of Aβ deposition

Aβ plaque burden and intensity of astrogliosis staining were calculated using the Positive Pixel Count program (Aperio). At least three sections per sample, 30 μm apart, were averaged by a blinded observer to calculate plaque burden. For CAA, three blinded observers reviewed the images and scored the extent of CAA based on the following criteria; "3" = more than 50% blood vessels have staining along the full circumference. "2" = 25%-50% of blood vessels have substantial staining. "1" = some blood vessels are stained with anti-pan Aβ biotinylated antibody. "0"—no staining observed in blood vessels.

3 | RESULTS

3.1 | Lysophosphatidyl glycerol and GM1 ganglioside micelles promote the formation of Aβ oligomers

Aβ oligomer formation was investigated in the presence of LPG micelles containing saturated 14 acyl carbon chain (C14:0 LPG) or 16 acyl carbon chain (C16:0 LPG) (Figure 1). Freshly purified Aβ monomer (50 μM) buffered in 20 mM Tris pH 8.0 and 50 mM NaCl was incubated with C14:0 or C16:0 LPG micelles and allowed to incubate at 37°C under quiescent conditions. The final concentration of LPG was kept at least two-fold above the reported critical micelle concentration (CMC) to ensure the lipids were in a micellar form.[54] After 48 hours of incubation, aliquots of the reactions were electrophoresed under partial denaturing conditions and visualized via immunoblotting, which revealed the presence of 30-60 kDa oligomers formed in the presence of LPG micelles along with some high molecular weight (HMW) bands (those that do not enter the gel) and monomers (Figure 1A). Immunoblot of the control reaction in the absence of LPG contains only a disperse oligomer band corresponding to ~200 kDa and fibrils that failed to enter the gel, suggesting that LPGs induce the formation of low molecular weight (LMW) Aβ oligomers (Figure 1A, lane C). Incubations of Aβ monomers (50 μM) in the presence of GM1 gangliosides in similar buffer and temperature conditions show oligomer bands with a bimodal molecular-weight distribution centered at ~40 and ~56 kDa, respectively (Figure 1A; GM1). Unlike LPG incubated reactions, no HMW fibrils were observed in the immunoblot of GM1-derived oligomers.

Fractionation of LPO incubated samples on a Superdex-75 column (Figure 1B-D) showed three Aβ species corresponding to monomers, oligomers, and fibrils similar to those observed in the immunoblots. Fractionation of the control sample in the absence of LPG or GM1 micelles (Figure 1B-D; dotted lines) showed only fibrils and monomers, further indicating that the oligomers are formed only in the presence of the lipids. Similar fractionation of Aβ incubated with GM1 showed predominantly two fractions (Figure 1E). Immunoblots of the fractionated 14LPOs and 16LPOs revealed that the peak close to the void volume (fraction 17) contained fibrils, as expected (Figure 1B-C; inset). The fractions eluting in more inclusive volumes at 18-20 contained the soluble oligomers (Figure 1B-C; inset), while monomers eluted in fractions at the most included volume (fraction 25). Similarly, immunoblots of GM1Os (Figure 1D) showed fractions 18-20 containing the oligomers (Figure 1D; inset), and notably, HMW aggregates in fraction 17 were absent (Figure 1D). Furthermore, the isolated oligomer samples electrophoresed under non-denaturing conditions (no heat; no SDS treatment) showed a differential migration pattern (based on m/z ratio) for GM1Os compared to other oligomers (Figure S1), which could suggest either the oligomer is different in size, charge or both, or the migration pattern is affected by the extent of lipid association in the oligomers.

Therefore, to investigate whether lipids are associated with isolated oligomers quantitatively, the samples were analyzed using electrospray ionization mass spectrometry (ESI-MS) in negative ion mode (Figure S2). Spectra of the controls, C14:0 LPG, C16:0 LPG, and GM1 in the absence of Aβ showed the presence of the –1 ion for both C14:0 and C16:0 LPGs at 455 and 483 m/z, respectively (Figure S2A,B). Multiple signals were observed with GM1 control (Figure S2C) corresponding to the varying sphingosine (denoted "d") and acyl moieties present in the commercial sample. This primarily included the 1545 ([(d18:1, C18:0) – 1H]-1) and 1573 ([(d20:1, C18:0) – 1H]-1) m/z ions, which have been observed previously.[55-57] Also observed were the 1612 and 1680 m/z ions, which were unassigned derivatives of GM1, consistent with the presence of multiple GM1 isoforms based on the manufacturer's note (Avanti Polar Lipids). Control Aβ reactions either for monomers or LFAOs yielded a 1503 m/z signal corresponding to the $[M - 3H]^{3-}$ Aβ ion (Figure S2D-E). The $[M - 3H]^{3-}$ Aβ ion was also observed in the isolated 14LPO and 16LPO

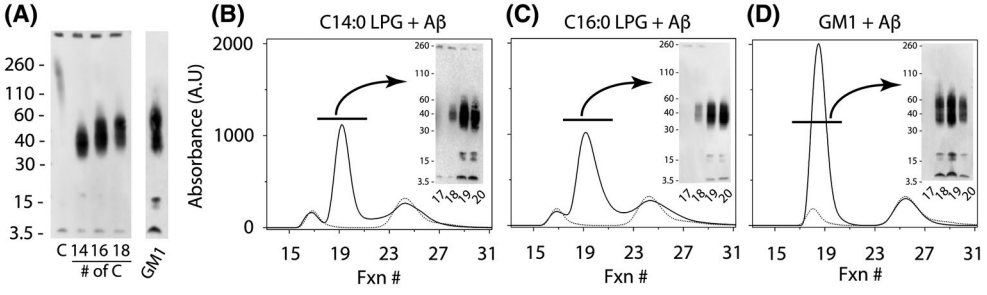

FIGURE 1 A, SDS-PAGE -immunoblots of the samples of Aβ (50-60 μM in 20 mM Tris, 50 mM NaCl, pH 8.0 and 0.01% NaN_3) incubated with C14:0 (400 μM), C16:0 (150 μM), and GM1 gangliosides (75 μM) lipid micelles above their critical micelle concentrations and imaged after 48 h of incubation. B-D, Fractionation of samples by SEC of the reactions in (A). The dotted lines are fractionation profiles of the control reaction in the absence of lipids. (*insets*; B-D) corresponding SDS-PAGE immunoblots of oligomeric fractions (denoted by the black line). Fraction numbers are labeled at the bottom of the gels

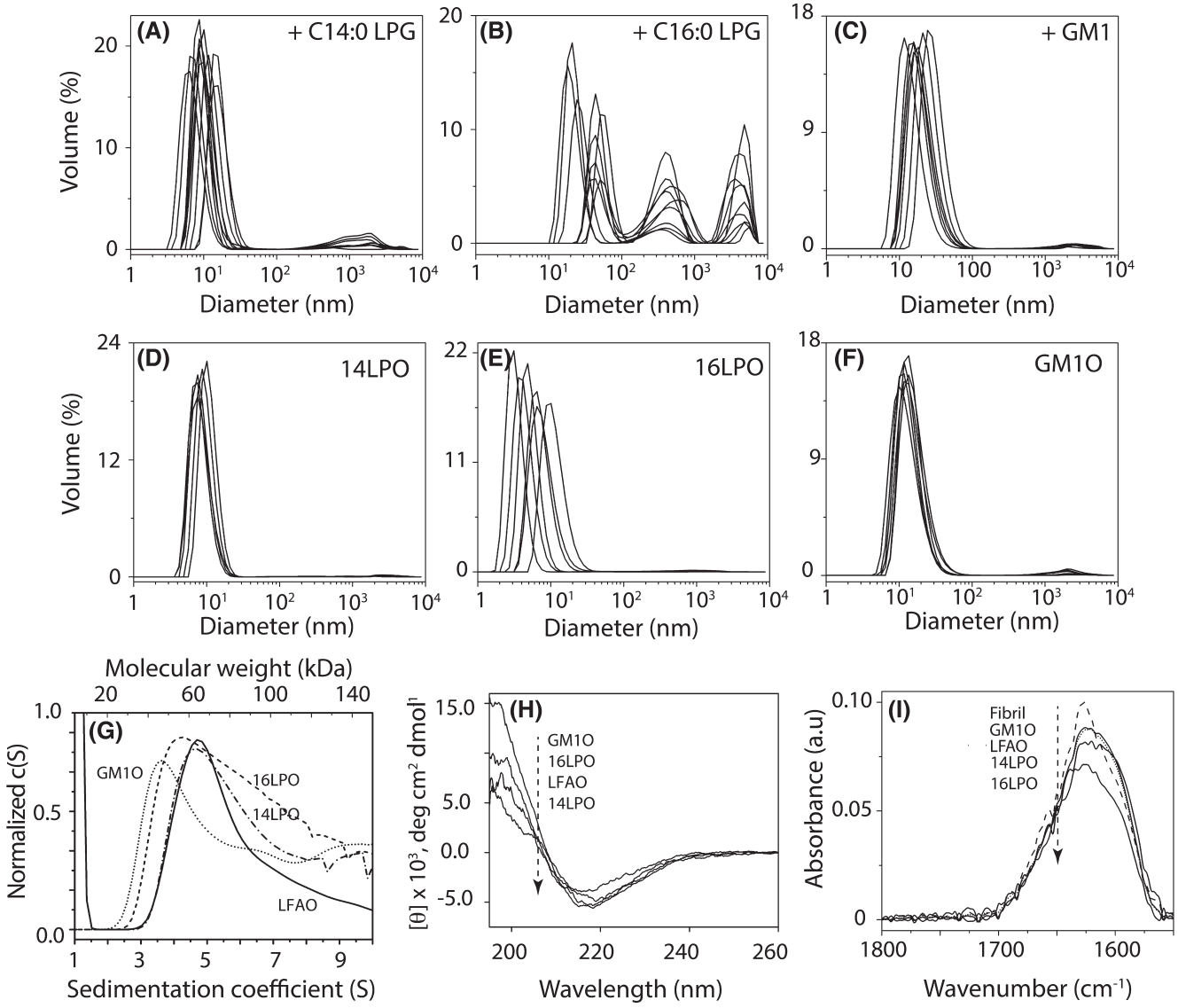

FIGURE 2 A-C, DLS size distribution profiles of oligomers weight by volume fractions from which hydrodynamic diameter (D_h) were determined. Shown are profiles for nine independent samples of 50-60 μM Aβ in 20 mM Tris, 50 mM NaCl at pH 8.0 and 0.01% NaN_3 incubated with (A) C14:0 LPG (B) C16:0 LPG, and (C) GM1 ganglioside micelles above their respective CMCs in the same buffer for 48 h. D-F, DLS size distribution profiles for the isolated oligomers after SEC fractionation (six independent samples): (D) 14LPOs. E, 16LPOs and (F) GM1Os. G, Size distribution based on sedimentation velocity experiments. H, Far UV circular dichroism of 10-16 μM samples of 14LPOs, 16LPOs, LFAOs, and GM1Os after SEC fractionation. I, FTIR spectra for 14LPOs, 16 LPOs, and GM1Os after SEC isolation along with fibril and LFAO controls.

samples but not the ones corresponding to the free C14:0 LPG (455 m/z) and C16:0 LPG (483 m/z) lipids (Figure S2F-G). This suggests that the isolated oligomers have an insignificant amount of lipid association similar to LFAOs as observed previously.[42] In contrast, isolated GM1Os showed the presence of GM1 gangliosides in the sample, and surprisingly no Aβ signals were observed (Figure S2H), suggesting that the lipids were associated with the isolated GM1Os. It is unclear as to why Aβ signals were not observed on the spectrum but it could be due to disruption in ionization caused by GM1 association. The presence of GM1 in isolated GM1Os was then quantified by HPLC (Figure S3), which revealed the presence of ~20% (molar) of GM1 lipid in the isolated GM1Os (2.5 μM in 12 μM oligomer sample).

3.2 | Biophysical characterization of oligomers

The size and secondary structure of micelle-derived oligomers, LPO and GM1O samples were analyzed by dynamic light scattering (DLS), circular dichroism (CD), and Fourier transform infrared (FTIR) spectroscopies (Figure 2). DLS size analysis of 14LPO, 16LPO, and GM1O samples before

SEC isolation revealed some degree of polydispersity with 14LPOs, a significant extent with 16LPOs, and a minimal extent with GM1Os (Figure 2A-C). Both 14LPOs and GM1Os contained predominant species with ~10 nm diameter and to a lesser extent large species >0.5 μm. Moreover, 16LPOs showed three distinct species between 10 nm and 10 μm. Fractionation of the oligomers by SEC resulted in more monodisperse isolated fractions centered around 10 nm in diameter (Figure 2D-F). Here too, 16LPOs showed variations in size between 5 and 10 nm between different preparations (Figure 2E). Unlike LPOs, both prior to and after SEC isolation, GM1Os displayed monodispersity with DLS spectra centered at 10 nm (Figure 2C,F), again suggesting that fibril formation may be minimal in the presence of GM1. This in turn suggests the possibility that the association of GM1 to Aβ could lead to a pathway different from fibril formation. Overall, the data suggest that all three oligomers have largely similar hydrodynamic diameters that are in the same range as of LFAOs,[42] which is consistent with the SEC and immunoblot data.

More stringent size estimates were performed by sedimentation velocity experiments. LFAOs showed a predominant species centered around 5S and a less abundant one around 7S (Figure 2G) corresponding to 60 and 110 kDa (12 and 24mers), respectively, which is consistent with our previous observation.[42] The 14LPOs and 16LPOs showed a sedimentation coefficient peak spread between 5S and 8S (~60-120 kDa) corresponding to 13-26mers (Figure 2G). The broad peak suggested heterogeneity especially in the 16LPO sample which the DLS data also indicates (Figure 2E). GM1Os showed relatively discrete peaks with a major species centered around 3S, along with minor ones at 6.5S and 9S that correspond to 9mers, 18mers, and to a lesser extent, 30mers, respectively (Figure 2G). The secondary structure of the oligomers was investigated by both far-UV CD and FTIR spectroscopy (Figure 2H,I). All oligomers showed CD spectra with a minimum at 217 nm indicative of β-sheet secondary structure (Figure 2H). To ascertain the type of the β-sheets (parallel or anti-parallel), FTIR spectra spanning the amide-I region was investigated (Figure 2I).[58] FTIR spectra of control fibrils formed in the absence of lipids (dashed line) and LFAOs (dotted line) showed an absorbance maximum at 1625 cm^{-1}, indicative of parallel β-sheets. Nearly identical spectra were observed for 14LPOs, 16LPOs, and GM1Os with a peak at 1620-1625 cm^{-1} (Figure 2I). Together with the absence of a peak at 1690 cm^{-1} indicates a parallel β-sheet structure for the samples. While these results differ with some reports of Aβ oligomers containing anti-parallel β-sheets,[59-61] they do parallel the observation for LFAOs,[44] which brings to focus a unifying characteristic among lipid-derived oligomers.

3.3 | Lipid-derived oligomers have ring-like morphology

Morphological features of the isolated oligomers were investigated by atomic force microscopy (AFM). All the oligomers showed morphology resembling spherical, punctate dots (Figure 3A,E,I). The 14LPO samples showed largely a uniform size with height centered at 1.5 nm with a few larger ones with 3.5 nm (Figure 3C). The 16LPO samples displayed a mixture of different sizes ranging between 2, 2.5, and 5 nm (Figure 3G), which is consistent with the heterogeneity observed in DLS (Figure 2E) and sedimentation velocity data (Figure 2G). GM1Os showed the most homogenous distribution of spherical particles with a height of 2.5-3.0 nm (Figure 3K), which is also consistent with DLS (Figure 2F). Sizes of these oligomers are slightly smaller than those observed for LFAOs which were 5-6 nm in height.[42,46] The phase images of the oligomers showed a presence of depression in the middle of the spherical dots, suggesting a ring- or a doughnut-shape for all the oligomers species (Figure 3B,F,J). The phase measurements were made as precise topographical analyses were limited by the large size of the AFM cantilever tip. The phase analysis describes the energy dissipation and how the tip interacts with the samples by detecting differences in the probe's oscillation in reference to the excitation oscillatory signal, while maintaining a constant amplitude. Physical features that would cause the phase lag to include differences in surface stiffness, viscoelasticity, adhesion, or topographical variations,[62] as we have shown previously.[46,63,64] The data thus derived were further confirmed by the cross-sectional analysis of the oligomers (Figure 3D,H,L), which is similar to those observed for LFAOs.[46]

3.4 | Stability of Aβ oligomers

Thermodynamic stability of the oligomers was determined by assessing their ability to resist denaturation by detergent (1% SDS) as a function of temperature. Upon the addition of SDS to the oligomers (1 μM), the conformational change from β-sheet to α-helix was monitored as a function of increasing temperature (Figure 4A-F). Panels a-e in Figure 4 show far-UV CD spectra for pre- and post-melted oligomers and fibrils at 10 and 90°C, respectively, which show this conformational transition. The melting profiles were generated by monitoring the transition at λ208 nm, while sweeping the temperature from 10 to 90°C. Oligomers and fibrils show two-state melting profiles with a sigmoidal denaturation pattern (Figure 4F). Up to ~40°C, no changes in the ellipticity was observed for any of the oligomers (Figure 4F), displaying their ability to resist denaturation at physiological temperatures. However, some distinguishable differences were observed in the denaturation

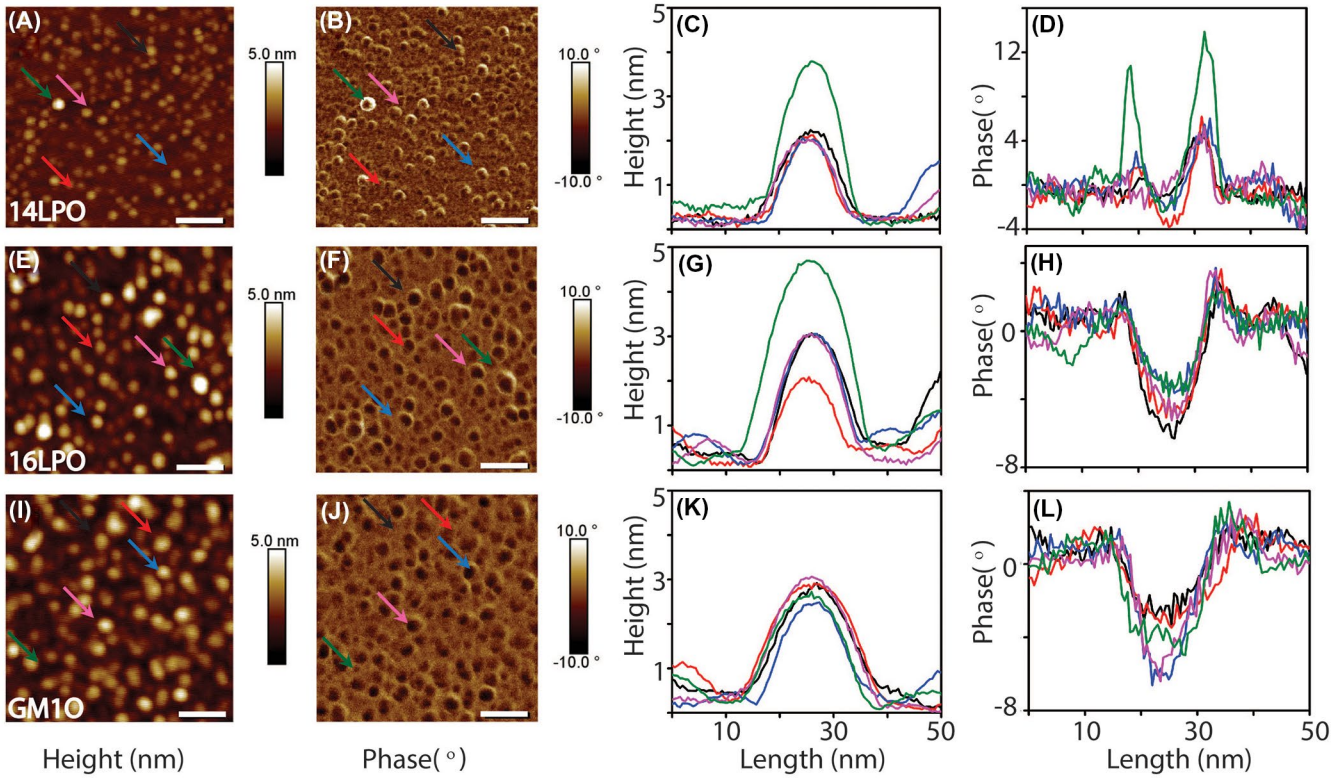

FIGURE 3 AFM height and phase images for 1-2 μM samples of freshly isolated oligomers samples imaged on a mica grid: (A-B) 14LPOs, (E-F) 16LPOs, (I-J) GM1Os. Scale bars represent 50 nm. Statistical height and phase analysis of AFM images for (C-D) 14LPOs, (G-H) 16LPOs, and (K-L) GM1Os

pattern among oligomers and fibrils. First, all oligomers melted into different degrees of α-helical structures as determined by the difference between ellipticities at wavelengths 222 and 208 nm. Although the debate on whether the relative intensity of ellipticity ($[\theta]$) between λ_{222} and λ_{208} indicates the extent of α-helix or 3_{10} helix seem to be unsettled,[65] it is clear that in the presence of SDS denaturant, helix displays a value of $[\theta]_{222} - [\theta]_{208} < 1.0$.[47-49] This criterion was used in normalizing the data (see Methods). Based on this analysis, GM1Os displayed complete melting followed by 14LPOs, while LFAOs and 16LPOs, which showed partial melting but to the same extent of the helix (Figure 4F). As expected, fibrils resisted melting to the largest extent with only ~25% of β-sheet melting into an α-helix (Figure 4F). Differences were also observed for the mid-point of transition corresponding to the melting temperature (T_m), defined as the temperature at which half of the protein is denatured ([N]/[D] = 0.5). From this analysis, GM1Os showed the lowest T_m with 60°C followed by 75, 69, and 70°C for 14LPOs, 16LPOs, and LFAOs, respectively. Further deconvolution of the data showed that the denaturation transition is largely entropy-driven for GM1Os as compared to others implicating the presence of exposed hydrophobic surfaces on the oligomers in part by the complexed lipid (Figure S3).

In parallel, the stability of oligomers toward enzymatic digestion was also probed by proteinase K (PK) treatment. The oligomers were incubated with (57 ng/mL) of PK and the stability was assessed based on the disappearance of the oligomer band from immunoblot as a function of time (Figure 4G,H). Each oligomer was incubated in small aliquots with PK in the buffer for 10, 20, 30, and 40 minutes and was subjected to electrophoresis on partially denaturing SDS-PAGE followed by western blotting with monoclonal antibody Ab5. With all oligomers, an immediate decrease in the band intensity and molecular weight was observed within 10 minutes of incubation as compared to the control (C) (Figure 4G). In addition to the reduction in oligomer band intensity, all oligomers except LFAO control resulted in the generation of fragmented monomers (Figure 4G; 3.0-4.0 kDa bands). A decrease in the oligomer band intensity was observed with an increase in the incubation time with PK (Figure 4H). All the oligomers showed nearly complete digestion within 20 minutes but GM1Os showed the most susceptibility to PK with complete digestion within 10 minutes (Figure 4H). These results indicate that all the oligomers show somewhat similar stability toward PK digestion. However, slightly increased susceptibility for GM1Os may suggest a less compact structural organization for GM1Os as compared to the other oligomers which parallel the thermal denaturation experiment observed (Figure 4F).

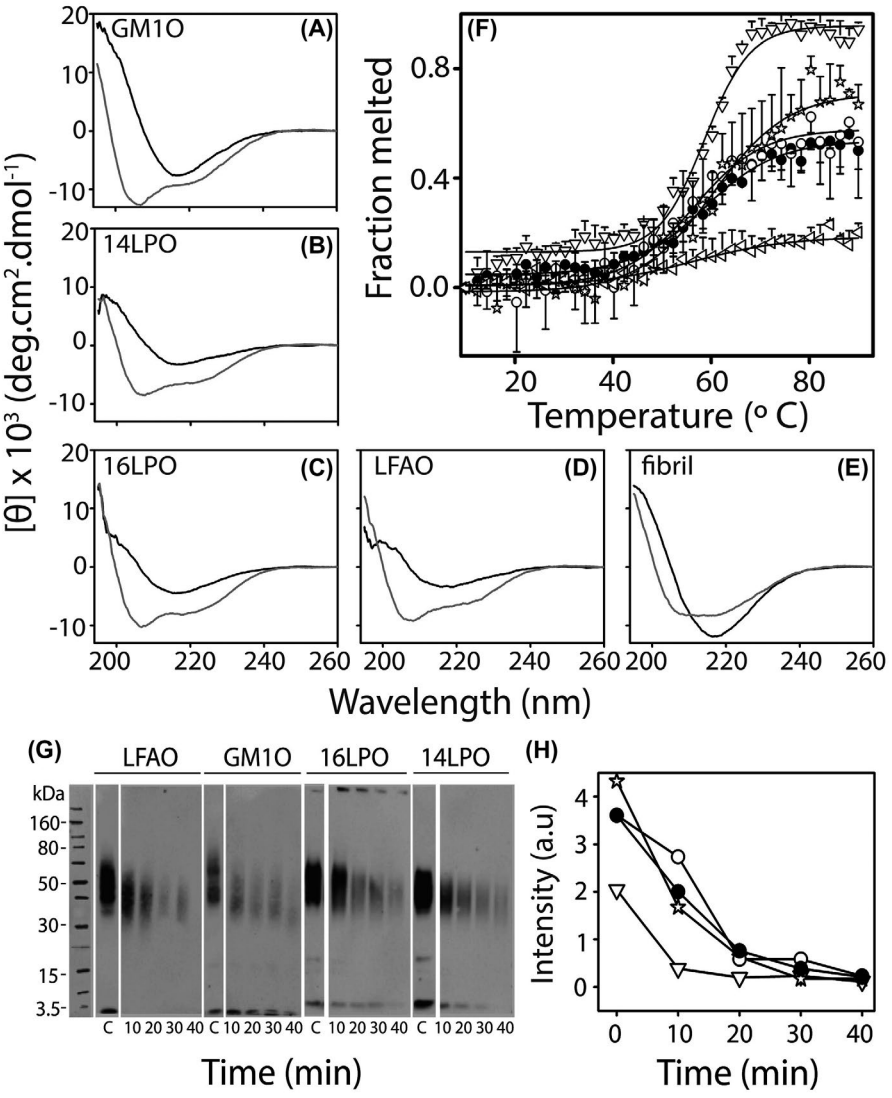

FIGURE 4 A-E, CD spectra of 1 μM GM1O, 14LPO, 16LPO, LFAO, and fibrils, respectively, before (black) and after (grey) their thermal denaturation (10-90°C) from β-sheet to α-helix in presence of 1% SDS. F, Normalized denaturation profiles obtained from CD spectra at 208 nm upon the addition of 1% SDS and increase in temperature from 10 to 90°C for: 14LPOs (●), 16LPOs (○), LFAOs (☆), GM1Os (□) and fibrils (◁). The spectra were fit with a Boltzmann's sigmoidal function. G, Partially denaturing SDS-PAGE -immunoblots of Aβ oligomers upon digestion with proteinase-K (PK) enzyme initiated with 1:2500 enzyme: protein ratio and monitored temporally for 10, 20, 30, and 40 minutes. C is the control reaction at 0 h without PK. H, Protein band intensities derived from (G) plotted as a function of time for GM1Os (□), LFAOs (☆), 16LPOs (○), and 14 LPOs (●)

3.5 | Conformation-sensitive dyes and antibodies reveal subtle structural differences among oligomers relatable to cytotoxicity

The natural product curcumin has been known to bind amyloid aggregates.[66-68] Recently, Condello and co-workers showed that curcumin discriminates between wild-type and mutant Aβ deposits derived from familial AD and CAA brain tissue based on the intensity and emission wavelength of the fluorescence spectrum.[66] Similarly, other fluorescent dyes such as polythiophenes have been shown to display different fluorescent properties upon binding to the sample tissues from varying etiological subtypes of AD.[17] We evaluated curcumin fluorescence in the presence of Aβ monomers, oligomers, and fibrils to explore if any differences in the spectroscopic properties could be discerned (Figure 5). The addition of curcumin (5 μM) to a solution of monomeric Aβ showed an emission spectrum centered at 560 nm (■; Figure 5A). All oligomers such as LFAOs, 14LPOs, 16LPOs, and GM1Os, as well as control fibrils, showed blue shifts to varying degrees, with GM1Os showing the maximal shift (Figure 5A,B). In addition, the oligomers showed variations in the intensity of florescence upon binding to the dye 8-anilino-1-naphthalenesulfonic acid (ANS), which is known to bind solvent-exposed hydrophobic surfaces (Figure 5C). LFAOs, 14LPOs, and 16LPOs showed identical increases in the intensity, while GM1Os showed nearly double the intensity compared to the rest of the oligomers (Figure 5C). We rule out that the increase is due to the lipid associated with GM1Os as compared to the blank lipid sample (data not shown). However, the contributions of lipid-induced structural changes leading to the exposure of hydrophobic surfaces cannot be ruled out. 1D ^{1}H NMR spectra of the amide region for the oligomers indicated significant differences in the spectra of GM1Os as compared to the others with many amide resonances shifted or unobserved (Figure 5D), suggesting different dynamics of conformational exchange and structure for the oligomers. Immunodetection by conformation-specific antibodies, A11 (oligomer-specific) and OC (fibril-specific) indicate that LFAOs, as previously known, and 14LPOs show OC-positivity (Figure 5E). While 16LPOs and GM1Os also

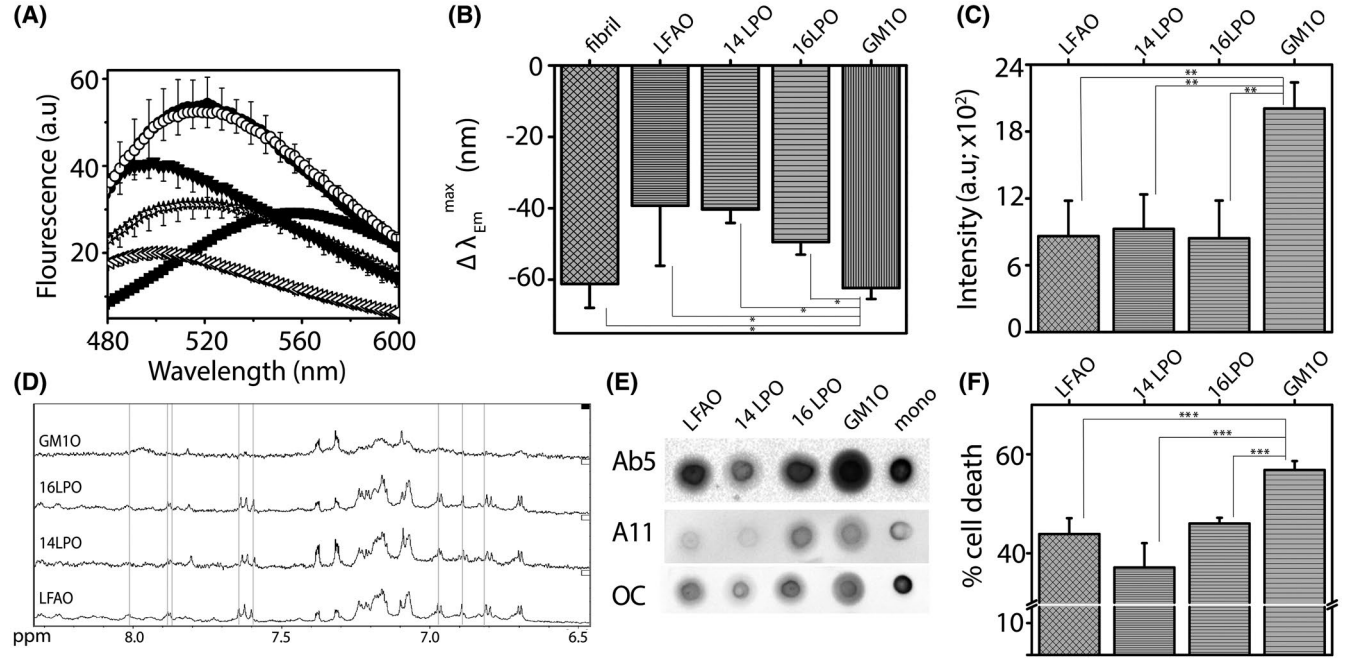

FIGURE 5 A, Normalized fluorescence emission scans for curcumin (5 μM in 25% EtOH) binding to 5-10 uM Aβ monomers (■), LFAOs (☆), 14LPOs (●), 16LPOs (○), GM1Os (▼), or fibrils (◁). B, Shifts in the emission maximum from that of the monomers ($\Delta\lambda_{Em}^{max}$) of the samples in (A). C, Blank corrected intensities of λ_{Em}^{max} for ANS dye (100 μM in 20 mM Tris pH 8.0) binding to 3 μM oligomers. D, 1D ^{1}H NMR spectra of the amide region for the oligomers that show backbone structural differences and similarities between the oligomers. E, Dot blots for the oligomers and monomers using sequence-specific Ab5 monoclonal antibody and conformation-specific monoclonal antibodies A11 (oligomer-specific) and OC (fibril-specific). F, Viability for SHSY5Y neuroblastoma cells measured by XTT assay upon incubating with oligomers expressed in terms of % of dead cells. n = 3 independent cell cultures on isolated oligomers; *, ** and *** $P < .05$ based on one-way ANOVA analysis

show OC-positive detection, they also showed a somewhat diminished A11-positive character (Figure 5E). To see whether the differences observed for GM1Os manifest in their cellular toxicities, the viability of SHSY5Y neuroblastoma cells upon treatment with the oligomers were investigated by XTT assay. After 40 hours of treatment, nearly 60% of the cells died due to GM1O exposure, while only ~40% were dead upon exposure with other oligomers (Figure 5F). Together, the data suggest that the biophysical differences between the oligomers correlate with their respective cellular toxicities.

3.6 | Lipid-derived Aβ oligomers show differential seeding resulting in morphologically different fibrils

Structural differences among oligomers often manifest in the morphology of their seeded fibrils. To see if the oligomers show differences in fibril morphologies generated upon seeding monomers, reactions were initiated by seeding Aβ monomer (25 μM) with 5 μM (20%) of 14LPOs (◇), 16LPOs (▽) or GM1Os (○) seeds individually. Reactions were buffered in 20 mM Tris (pH 8.0) with 50 mM NaCl and were maintained under quiescent conditions at 37°C. The aggregation reactions were deliberately initiated with high seed amounts (20%) and under quiescent conditions to minimize nucleated aggregation reaction among monomers and to maximize templated, seeded aggregation by the oligomers. The samples were centrifuged after 30 days of incubation at 37°C, and the sedimented pellets were washed with buffer and subjected to analysis by AFM. Samples for 14LPOs, 16LPOs, and GM1Os showed fairly smooth fibrils on the mica grid (Figure 6A,D,G, respectively). Detailed analysis of the morphologies, however, revealed that both 14LPO-seeded and 16LPO-seeded fibrils displayed periodic repeats of crests and troughs along the length of the fibril (Figure 6A,D; white arrows) with 3.0-4.5 nm heights (Figure 6B,E; right panels). These heights are identical to those observed for individual oligomers (Figure 3), leading us to conjecture that the fibrils were comprised of individual oligomer units that give rise to "repeat morphology." Identical morphology was observed previously for LFAO-seeded fibrils.[9] The cross-sectional analysis perpendicular to the fibril axis (colored lines) showed heights of ~4.0 and 6.0 nm for 14LPO-seeded and 16LPO-seeded fibrils, respectively (Figure 6D,G; right panels). This was consistent in many different fields in the mica grid (Figure 6J). In sharp contrast, GM1O-seeded fibrils did not show such a repeat morphology but showed a cross-sectional height of ~5 nm (Figure 6G,H,I,I). Together, these results indicate that both 14LPOs and 16LPOs are able to generate fibrils of similar morphologies, GM1Os showed significant deviations both in temporal profiles and fibril morphology.

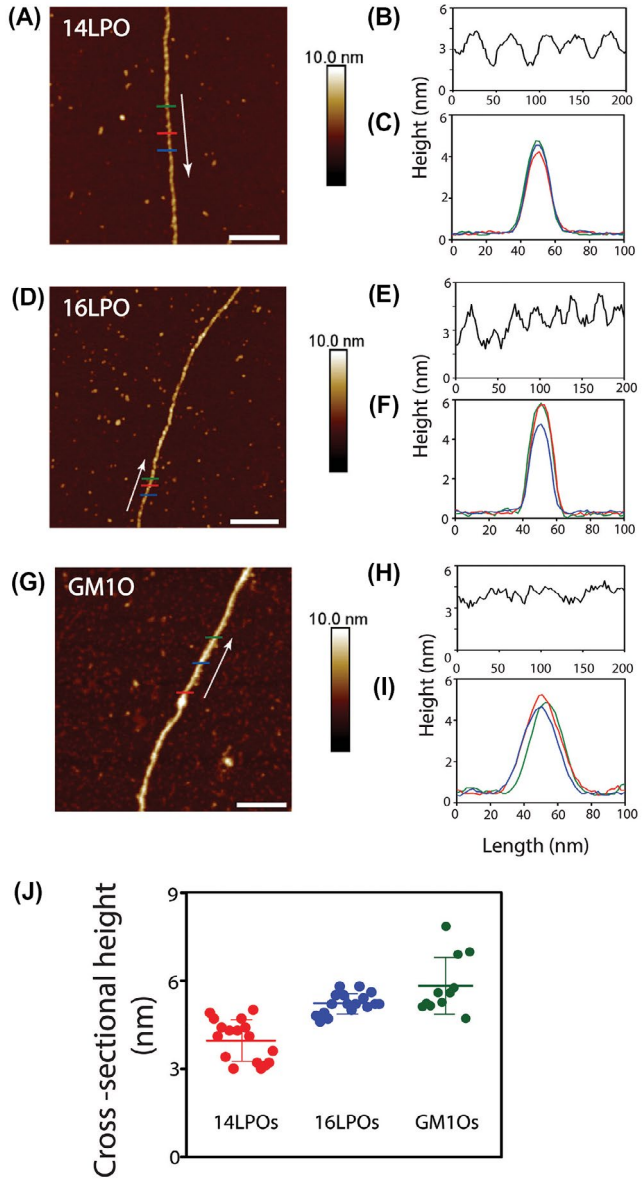

FIGURE 6 A, D, G, AFM images of Aβ fibrils generated from obtained from aggregation kinetics of Aβ monomers (25 μM) seeded with 5 μM of 14LPOs, 16LPOs or GM1Os in 20 mM Tris, pH 8.0, with 50 mM NaCl and 50 μM ThT at 37°C under quiescent conditions after 30 days of incubation. Scale bar is 200 nm. Statistical height analysis along cross-sectional and longitudinal axes on the AFM images indicated by colored lines and arrows, respectively, for; (B-C) 14LPO-seeded, (E-F) 16LPO-seeded, and (H-I) GM1O-seeded fibrils. J, Cross-sectional height analysis of the fibrils visualized on at least twelve different fields from at least three independent data sets. The data obtained from these also show no "repeat morphology" for GM1Os, unlike other two oligomers

3.7 | Aβ oligomers injection into Tg CRND8 mice induce amyloid pathology and vascular amyloid deposition

Based on the aforementioned biophysical data and the previously observed effects of LFAOs on amyloid accumulation and CAA formation in CRND8 mice,[9] we set to test whether the introduction of the oligomers to the neonatal brains of AD transgenic mice will result in the extended propagation of oligomers and fibril deposition. Thus, 4 μL of 10 μM preparations of 14LPOs, 16LPOs, and GM1Os along with Aβ42 monomers and LFAOs as controls were bilaterally injected into the cerebral ventricles of three litters of newborn Tg CRND8 mice. After three months, the mice were euthanized and brains were extracted. One hemibrain was frozen for further biochemical analysis, while the other was fixed in 4% paraformaldehyde, paraffin-embedded, and processed for immunostaining. Upon analysis, the control mice injected with Aβ42 monomer exhibited a sparse number of small amyloid deposits both in the cortex and hippocampus, whereas the injection of LFAO resulted in increased levels of Aβ40 and Aβ42 in both SDS and formic acid (FA) fractions similarly to what was shown in (Figure 7A-F).[9] LFAO administration also expedited the accumulation of amyloid in the CAA as previously observed (Figure 7G,I).[9] Interestingly, injection of 14LPOs did not alter Aβ levels in the SDS fraction significantly but did so in the FA-soluble fractions, suggesting that the oligomers induced insoluble fibrils deposition. It also did not affect the accumulation of CAA in the vasculature. In contrast, 16LPO injection resulted in increased levels of Aβ42 in SDS-soluble fraction as well as increased Aβ40 and Aβ42 in FA-soluble fraction. The oligomers also induced an increased burden of CAA-laden vessels (Figure 7G,I). GM1O administration to neonatal CRND8 mice also resulted in increased Aβ levels in both SDS and FA fractions, similar to LFAOs and 16LPOs (Figure 7C-F). Overall, we demonstrate a twofold increase in Aβ40 and Aβ42 in SDS-soluble and SDS-insoluble FA-soluble fractions of GM1Os compared to the monomer control. Furthermore, GM1Os induced widespread CAA in cerebral vasculature and overall Aβ burden (Figure 7G-I). However, injection of all the oligomers samples at lower concentrations (1 μM) did not result in significant amyloid accumulation in the brains (Figure S5). Together, these suggest that LFAOs, 16LPOs, and GM1Os propagate and induce amyloid deposition in parenchyma and cerebral vasculature with GM1Os and 16LPOs showing the maximal effect.

4 | DISCUSSION

Monomeric Aβ peptides self-associate to form large fibrillar aggregates that deposit as insoluble, protease-resistant plaques in AD. NMR structures of fibrils propagated in vitro using brain-derived amyloid seeds as templates have revealed structural differences between morphologically distinguishable aggregates.[15,69] Similarly, conformation sensitive fluorescent dyes have also identified the presence of heterogeneous

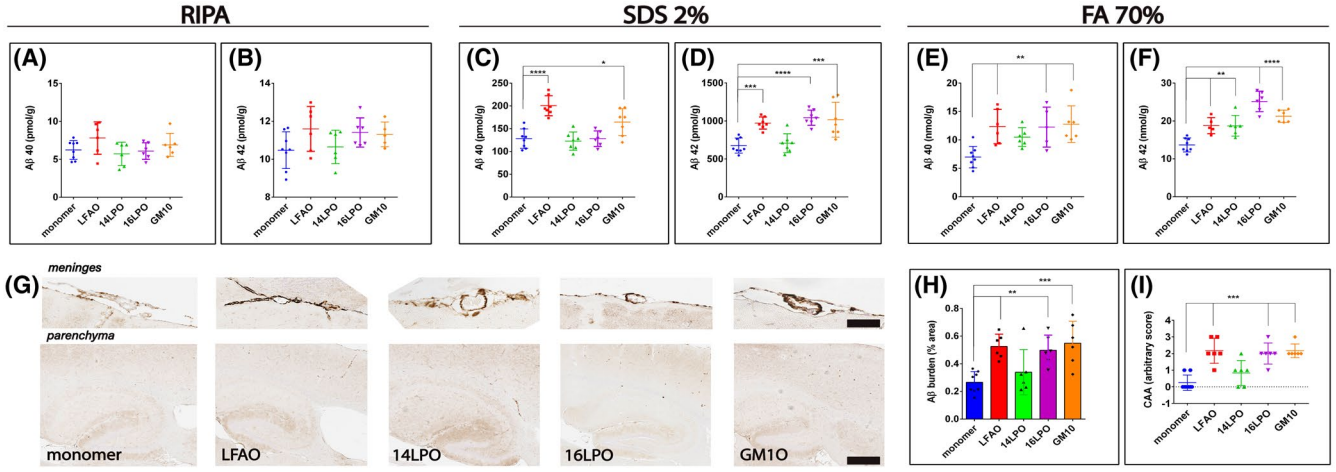

FIGURE 7 Oligomers induce widespread amyloid deposition and CAA in TgCRND8 mice. Newborn CRND8 mice were injected with 4 µL aliquots of Aβ42 monomers, LFAOs, 14LPOs, 16LPOs, and GM1Os (10 µM) in the cerebral ventricles. Three months later, brains were extracted and one hemibrain was frozen, while another was fixed and stained with anti-pan- Aβ mAb5 Biotin antibody. A-F, Biochemical analyses of sequentially extracted Aβ42 and Aβ40 levels by end-specific sandwich ELISA show significantly increased SDS soluble and FA soluble Aβ levels in LFAOs, 16LPOs, and GM1Os injected mice compared to monomer injected mice. Data represent mean ± sem. n = 6-10 mice per group. N = 6-10, $*P < .05$, $**P < .01$, $***P < .001$, $****P < .0001$, one-way ANOVA). G, Amyloid staining of plaques and CAA in the representative paraffin sections is shown in the cortex and meningeal vessels of injected mice. Scale Bar, 500 µm (cortex), 100 µm (hippocampus). H, Quantification of Aβ positive immunostaining shows significantly increased amyloid plaque burden (immunostained with anti-pan-Aβ mAb5Biotin). Data represent mean ± SEM. n = 6-10/group. $**P < .01$, $***P < .001$, one-way ANOVA. I, Quantification of CAA. Aβ positive blood vessels in the meninges and throughout the brain tissue were evaluated in a blind manner and given a qualitative score from 0 to 3. Vessels with scores 0, 1, 2 or 3 were counted. Data represent mean ± sem. n = 6-10 per group. $***P < .001$, one-way ANOVA

aggregate conformations in the brain that correlate with diverse phenotypes in AD such as those corresponding to late or early onset, rapidly progressing or anatomical region of deposition.[17,66] Top-down discoveries such as these have unequivocally established that differences in aggregate structures may lead to different phenotypes in the brain. Since low molecular weight soluble oligomers are known to be the primary toxic species in the aggregation pathway, a question then arises as to whether conformationally distinct oligomers are capable of faithful propagation of their structures toward distinguishable fibril morphologies, and if so, whether such a propagation will manifest in phenotypic differences in the AD brains. Here, we approached to answer this question bottom-up by generating distinct oligomer sub-types and correlating their biophysical properties with observable effects in transgenic AD mice brains. We have earlier demonstrated that LFAOs generated in the presence of fatty acid propagate their structure toward distinct fibrils on the mesoscopic scale and selectively induce CAA in a transgenic AD mouse model.[9] Here, we used micelle forming phospholipids and a sphingolipid to generate stable oligomers, characterize their biophysical differences and similarities, and correlate them with the phenotypes induce in C8ND8 mice.

The results obtained here bring forth several salient inferences. First, the micellar anionic phospholipids promote the formation of disperse ~60-120 kDa (5-8S) Aβ42 oligomers, which corresponds to a 12-26mer species. Despite being somewhat heterogenous, this size is comparable to the earlier characterized LFAOs,[42] which suggests that the carbon chain length variations (12, 14, or 16 carbon acyl chains) do not seem to have a noticeable effect on the size of the oligomer generated. However, LFAOs were generated with fatty acid near its CMC and not above, which implicates the significance of micelles in the case of phospholipids. Second, micelles of the neutral sphingolipid GM1 ganglioside induce the formation of slightly smaller and more discrete ~40 and 80 kDa (3 and 6.5 S) species corresponding to 9 and 18mers. The slightly different sizes obtained from GM1 lipids could be attributed to neutral charge, longer acyl chains (18,20), carbohydrate moiety, or all three.

Among the isolated oligomers reported here, GM1Os stand out as a distinct outlier on the observed biophysical and biochemical attributes. GM1Os do share similarities on parallel β-sheet secondary structure and a ring-like morphology as well as the size range. However, they show stark biophysical differences too (Figure 8). For example, the amide region of the ^{1}H NMR spectra indicates structural dynamics and assembly differences in GM1Os which is corroborated by the greater degree of exposed hydrophobic surfaces by ANS binding and decreased enzymatic and thermal stabilities. Similarly, GM1Os and 16LPOs show reactivity toward both conformation-specific A11 and OC antibodies unlike the

other two which show only OC specificity. Such differences are also manifested in their ability to propagate morphologically distinct fibrils; 14LPOs and 16LPOs but not GM1Os, generate fibrils containing a "repeat" morphological feature similar to LFAOs.[9] These observations are summarized in Figure 8 that show biophysical differences among the oligomers investigated in this study. Such biophysical differences also have direct and correlatable manifestations in vivo. Cell viability assays indicate that GM1Os to be the most potent in cellular toxicity as compared to the other oligomers. Similarly, in CRND8 mice too, GM1Os showed profound effects on both the induction of total Aβ burden and CAA. Surprisingly, despite significant biophysical differences, GM1Os, 16LPOs, and LFAOs show high but comparable effects on amyloid deposition in CRND8 mice.

There can be several features within the lipid that are attributable to the generation of Aβ oligomers and their observed properties. It is possible that the development of pathology following Aβ seeding depends tightly on the size and solubility of initial seeds and not on their biochemical properties.[70] The oligomers compared here have somewhat similar sizes; however, the lipid characteristics are different; in comparison to the anionic LPGs used in this study, GM1 gangliosides differ in acyl chain lengths, charge, and head groups, which may confer GM1Os their distinctive properties. A recent report on the interactions of Aβ with synthetic glycopolymer mimics revealed the selective induction of Aβ oligomers by glycopolymers containing purely glucose pendant groups,[71] which implicates that sugar distribution in GM1 ganglioside is important for oligomer generation. In addition, ~20% of isolated GM1Os contain GM1 lipid which could also have a role to play in their behavior in mice. The increased hydrophobic character is consistent with the lipid-bound oligomer form, which may manifest in its lipid solubility, bioavailability, and seeding in vivo. It is also rational to conjecture that a stable oligomer strain is more likely to be present in a lipid-bound form than in a purely homogenous form. Such a contention is also consistent with earlier reports on Aβ oligomers isolated from postmortem AD brains that were associated with GM1 gangliosides.[28,29] GM1 gangliosides are important components of lipid rafts that have been known to play important roles in AD.[30] Therefore, it is comprehensible that lipid association to the isolated GM1Os could play a role in their biophysical and biochemical distinctions. The slightly decreased PK stability of GM1Os seems to be counter-intuitive to their effect on mice brains. It is possible that the lipid association is partly responsible for the exposure of polypeptide backbone for increased enzymatic cleavage, but the lipid association could also increase the lipophilicity of the oligomers to effectively propagate in parenchyma, meninges, and cerebrospinal fluid.

The results presented here demonstrate that oligomers with distinct properties can be tuned by changing the physiochemical properties of lipids and support the hypothesis that varying lipid environments could play important roles in the generation of conformeric oligomer strains.[72] Along the same lines, these also lead to the conjecture that while oligomers may have different structures to present themselves as conformational "strains," they may also possess common features and traits such as those observed for oligomers derived from anionic lipids. Despite the numerous challenges these oligomers present, understanding the atomic details of their structures would be essential to further decipher their mechanisms and functions. Furthermore, understanding the physiological relevance of lipid-derived oligomers by investigating their in vivo behavior in detail would be essential. In addition, the ability of these oligomers to propagate cell-to-cell transmissions needs to be assessed to assess their propensity to truly behave like infectious prions or "strains".[73-76] Although the in vitro oligomers presented here clearly show pathology in mice, ascertaining whether and how they represent those present in human brains is important. Recent reports on the structure of in vitro fibrils generated by the propagation of brain-derived seeds have made a significant

	size	secondary structure	backbone conformation	dye binding	immuno-detection	morphology		stability		cell viability	effect on CRND8 mice	
						oligomer	fibrils	temperature	PK			
	(mers)	parallel β-sheet		ANS / curcumin		ring-like	repeat	T_m(°C)			Aβ burden	CAA
LFAOs	= (12; 24)	=	=	=	OC	=	=	70	=	=	=	=
14LPOs	= (13-26)	=	=	=	OC	=	=	75	=	=	low	low
16LPOs	= (13-26)	=	=	=	OC, A11	=	=	69	=	=	high	high
GM1Os	≠ (9; 18)	=	≠	≠	OC, A11	=	≠	60	≠	≠	high	high

FIGURE 8 Summary of results indicating the differences and similarities between the oligomers. The grey boxes indicate the salient differences in GM1Os as compared to the others; "=" and "≠", respectively, indicate similar or dissimilar to other oligomers

leap in this regard. However, it is non-trivial to investigate oligomers derived from brain samples due to their transiency, heterogeneity, and difficulty to isolate. Despite these issues, characterizing them continues to remain as a major focus in ours and other laboratories. Nevertheless, the data presented here as such showcase the generation of biophysically distinct oligomers by modulating the lipid characteristics, and one that correlates to their biochemical proprieties in vivo. Establishing such structure-phenotype correlations are imperative to decipher the mechanisms by which oligomers impart strain-like properties.

ACKNOWLEDGMENTS

The authors would like to thank the following agencies for financial support: National Institute of Aging (1R56AG062292-01), National Institute of General Medical Sciences (R01GM120634), and the National Science Foundation (NSF CBET 1802793) to VR, NSF Graduate Research Fellowship Program (NSF 1445151) to DND and NSF NRT (NRT 1449999) to KAS. The authors also thank the National Center for Research Resources (5P20RR01647-11) and the National Institute of General Medical Sciences (8 P20 GM103476-11) from the National Institutes of Health for funding through INBRE for the use of their core facilities. The authors also thank Dr Claudius Mundoma and FSU Physical Biochemistry facility for their generous help in collecting AUC data.

CONFLICT OF INTEREST

The authors declare no conflicts of interest.

AUTHOR CONTRIBUTIONS

V. Rangachari conceptualized the paper, J. Saha and D.N. Dean performed biophysical experiments, S. Dhakal performed cellular toxicity assays, K.A. Stockmal and S.E. Morgan performed M.F. Adamo experiments, K.D. Dillon, M.F. Adamo, and Y. Levites performed transgenic mice experiments. All authors contributed to manuscript writing but were mainly performed by J. Saha, D.N. Dean, and V. Rangachari. All authors have given approval to the final version of the manuscript.

REFERENCES

1. Selkoe DJ. Alzheimer's disease: genes, proteins, and therapy. *Physiol. Rev*. 2001;81:741-766.
2. Westerman MA, Cooper-Blacketer D, Mariash A, et al. The relationship between Abeta and memory in the Tg2576 mouse model of Alzheimer's disease. *J Neurosci*. 2002;22:1858-1867.
3. Billings LM, Oddo S, Green KN, McGaugh JL, LaFerla FM. Intraneuronal Abeta causes the onset of early Alzheimer's disease-related cognitive deficits in transgenic mice. *Neuron*. 2005;45:675-688.
4. Gong Y, Chang L, Viola KL, et al. Alzheimer's disease-affected brain: presence of oligomeric Aβ ligands (ADDLs) suggests a molecular basis for reversible memory loss. *Proc Natl Acad Sci*. 2003;100:10417-10422.
5. Haass C, Selkoe DJ. Soluble protein oligomers in neurodegeneration: lessons from the Alzheimer's amyloid β-peptide. *Nat Rev Mol Cell Biol*. 2007;8:101-112.
6. Jongbloed W, Bruggink KA, Kester MI, et al. Amyloid-beta oligomers relate to cognitive decline in Alzheimer's disease. *J Alzheimer's Dis*. 2015;45:35-43.
7. McLean CA, Cherny RA, Fraser FW, et al. Soluble pool of Abeta amyloid as a determinant of severity of neurodegeneration in Alzheimer's disease. *Ann Neurol*. 1999;46:860-866.
8. Lue LF, Kuo YM, Roher AE, et al. Soluble amyloid beta peptide concentration as a predictor of synaptic change in Alzheimer's disease. *Am J Pathol*. 1999;155:853-862.
9. Dean DN, Das PK, Rana P, et al. Strain-specific fibril propagation by an Aβ dodecamer. *Sci Rep*. 2017;7:40787.
10. Petkova AT, Leapman RD, Guo Z, Yau WM, Mattson MP, Tycko R. Self-propagating, molecular-level polymorphism in Alzheimer's beta-amyloid fibrils. *Science*. 2005;307:262-265.
11. Kodali R, Williams AD, Chemuru S, Wetzel R. Aβ(1–40) forms five distinct amyloid structures whose β-sheet contents and fibril stabilities are correlated. *J Mol Biol*. 2010;401:503-517.
12. Watanabe-Nakayama T, Ono K, Itami M, Takahashi R, Teplow DB, Yamada M. High-speed atomic force microscopy reveals structural dynamics of amyloid beta1-42 aggregates. *Proc Natl Acad Sci USA*. 2016;113:5835-5840.
13. Walker LC. Proteopathic strains and the heterogeneity of neurodegenerative diseases. *Annu Rev Genet*. 2016;50:329-346.
14. Yates EA, Legleiter J. Preparation protocols of abeta(1–40) promote the formation of polymorphic aggregates and altered interactions with lipid bilayers. *Biochemistry*. 2014;53:7038-7050.
15. Lu JX, Qiang W, Yau WM, Schwieters CD, Meredith SC, Tycko R. Molecular structure of beta-amyloid fibrils in Alzheimer's disease brain tissue. *Cell*. 2013;154:1257-1268.
16. Cohen ML, Kim C, Haldiman T, et al. Rapidly progressive Alzheimer's disease features distinct structures of amyloid-beta. *Brain*. 2015;138:1009-1022.
17. Rasmussen J, Mahler J, Beschorner N, et al. Amyloid polymorphisms constitute distinct clouds of conformational variants in different etiological subtypes of Alzheimer's disease. *Proc Natl Acad Sci USA*. 2017;114:13018-13023.
18. Condello C, Lemmin T, Stöhr J, et al. Structural heterogeneity and intersubject variability of Aβ in familial and sporadic Alzheimer's disease. *Proc Natl Acad Sci*. 2018;115:E782-E791.
19. Qiang W, Yau W-M, Lu J-X, Collinge J, Tycko R. Structural variation in amyloid-β fibrils from Alzheimer's disease clinical subtypes. *Nature*. 2017;541:217-221.
20. Planchard MS, Samel MA, Kumar A, Rangachari V. The natural product betulinic acid rapidly promotes amyloid-β fibril formation at the expense of soluble oligomers. *ACS Chem Neurosci*. 2012;3:900-908.
21. Arosio P, Knowles TP, Linse S. On the lag phase in amyloid fibril formation. *Phys Chem Chem Phys*. 2015;17:7606-7618.
22. Kumar A, Bullard RL, Patel P, et al. Non-esterified fatty acids generate distinct low-molecular weight amyloid-β (Aβ42) oligomers along pathway different from fibril formation. *PLoS ONE*. 2011;6:e18759.
23. Colin J, Gregory-Pauron L, Lanhers MC, et al. Membrane raft domains and remodeling in aging brain. *Biochimie*. 2016;130:178-187.

24. Naudi A, Cabre R, Jove M, et al. Lipidomics of human brain aging and Alzheimer's disease pathology. *Int Rev Neurobiol*. 2015;122:133-189.
25. Noel A, Ingrand S, Barrier L. Ganglioside and related-sphingolipid profiles are altered in a cellular model of Alzheimer's disease. *Biochimie*. 2017;137:158-164.
26. Kiskis J, Fink H, Nyberg L, Thyr J, Li JY, Enejder A. Plaque-associated lipids in Alzheimer's diseased brain tissue visualized by nonlinear microscopy. *Sci Rep*. 2015;5:13489.
27. Morgado I, Garvey M. Lipids in amyloid-beta processing, aggregation, and toxicity. *Adv Exp Med Biol*. 2015;855:67-94.
28. Yanagisawa K, Odaka A, Suzuki N, Ihara Y. GM1 ganglioside-bound amyloid beta-protein (A beta): a possible form of preamyloid in Alzheimer's disease. *Nat Med*. 1995;1:1062-1066.
29. Yanagisawa K, Ihara Y. GM1 ganglioside-bound amyloid beta-protein in Alzheimer's disease brain. *Neurobiol Aging*. 1998;19:S65-67.
30. Tettamanti G, Anastasia L. Chemistry, tissue and cellular distribution, and developmental profiles of neural sphingolipids. In: Lajtha A, Tettamanti G, Goracci G, eds. *Handbook of Neurochemistry and Molecular Neurobiology: Neural Lipids*. Boston, MA: Springer; 2010:99-171.
31. Choo-Smith LP, Garzon-Rodriguez W, Glabe CG, Surewicz WK. Acceleration of amyloid fibril formation by specific binding of Abeta-(1–40) peptide to ganglioside-containing membrane vesicles. *J Biol Chem*. 1997;272:22987-22990.
32. Ariga T, Kobayashi K, Hasegawa A, Kiso M, Ishida H, Miyatake T. Characterization of high-affinity binding between gangliosides and amyloid beta-protein. *Arch Biochem Biophys*. 2001;388:225-230.
33. Matsuzaki K, Horikiri C. Interactions of amyloid beta-peptide (1–40) with ganglioside-containing membranes. *Biochemistry*. 1999;38:4137-4142.
34. Kakio A, Nishimoto S, Yanagisawa K, Kozutsumi Y, Matsuzaki K. Interactions of amyloid beta-protein with various gangliosides in raft-like membranes: importance of GM1 ganglioside-bound form as an endogenous seed for Alzheimer amyloid. *Biochemistry*. 2002;41:7385-7390.
35. Kakio A, Nishimoto SI, Yanagisawa K, Kozutsumi Y, Matsuzaki K. Cholesterol-dependent formation of GM1 ganglioside-bound amyloid beta-protein, an endogenous seed for Alzheimer amyloid. *J Biol Chem*. 2001;276:24985-24990.
36. Choo-Smith LP, Surewicz WK. The interaction between Alzheimer amyloid beta(1–40) peptide and ganglioside GM1-containing membranes. *FEBS Lett*. 1997;402:95-98.
37. Terzi E, Holzemann G, Seelig J. Self-association of beta-amyloid peptide (1–40) in solution and binding to lipid membranes. *J Mol Biol*. 1995;252:633-642.
38. Terzi E, Holzemann G, Seelig J. Interaction of Alzheimer beta-amyloid peptide(1–40) with lipid membranes. *Biochemistry*. 1997;36:14845-14852.
39. Bokvist M, Lindström F, Watts A, Gröbner G. Two types of Alzheimer's β-amyloid (1–40) peptide membrane interactions: aggregation preventing transmembrane anchoring versus accelerated surface fibril formation. *J Mol Biol*. 2004;335:1039-1049.
40. Rangachari V, Moore BD, Reed DK, et al. Amyloid-beta(1–42) rapidly forms protofibrils and oligomers by distinct pathways in low concentrations of sodium dodecylsulfate. *Biochemistry*. 2007;46:12451-12462.
41. Barghorn S, Nimmrich V, Striebinger A, et al. Globular amyloid beta-peptide oligomer - a homogenous and stable neuropathological protein in Alzheimer's disease. *J Neurochem*. 2005;95:834-847.
42. Kumar A, Paslay LC, Lyons D, Morgan SE, Correia JJ, Rangachari V. Specific soluble oligomers of amyloid-β peptide undergo replication and form non-fibrillar aggregates in interfacial environments. *J Biol Chem*. 2012;287:21253-21264.
43. Kumar A, Pate KM, Moss MA, Dean DN, Rangachari V. Self-propagative replication of abeta oligomers suggests potential transmissibility in Alzheimer disease. *PLoS ONE*. 2014;9:e111492.
44. Dean DN, Pate KM, Moss MA, Rangachari V. Conformational dynamics of specific Aβ oligomers govern their ability to replicate and induce neuronal apoptosis. *Biochemistry*. 2016;55:2238-2250.
45. Dean DN, Rana P, Campbell RP, Ghosh P, Rangachari V. Propagation of an Aβ dodecamer strain involves a three-step mechanism and a key intermediate. *Biophys J*. 2018;114:539-549.
46. Xi W, Dean DN, Stockmal KA, Morgan SE, Hansmann UH, Rangachari V. Large fatty acid-derived A β 42 oligomers form ring-like assemblies. *J Chem Phys*. 2019;150:075101.
47. Chemes LB, Alonso LG, Noval MG, de Prat Gay G.Circular Dichroism Techniques for the Analysis of Intrinsically Disordered Proteins and Domains In: Uversky V., Dunker A. (eds) Methods in Molecular Biology (Methods and Protocols)895Humana Press: Totowa, NJ; 2012 https://doi.org/10.1007/978-1-61779-927-3_22.
48. Kaspersen JD, Søndergaard A, Madsen DJ, Otzen DE, Pedersen JS. Refolding of SDS-unfolded proteins by nonionic surfactants. *Biophys J*. 2017;112:1609-1620.
49. Hou H, He H, Wang Y. Effects of SDS on the activity and conformation of protein tyrosine phosphatase from thermus thermophilus HB27. *Sci Rep*. 2020;10:1-8.
50. Van Holde KE, Weischet WO. Boundary analysis of sedimentation-velocity experiments with monodisperse and paucidisperse solutes. *Biopolymers*. 1978;17:1387-1403.
51. Santacruz K, Lewis J, Spires T, et al. Tau suppression in a neurodegenerative mouse model improves memory function. *Science*. 2005;309:476-481.
52. Sacino AN, Brooks M, McGarvey NH, et al. Induction of CNS α-synuclein pathology by fibrillar and non-amyloidogenic recombinant α-synuclein. *Acta Neuropathol Commun*. 2013;1:38.
53. Howard AJ, Williams HM. The prevalence of antibiotic resistance in Haemophilus influenzae in Ireland. *J Antimicrob Chemother*. 1989;24:963-971.
54. Stafford RE, Fanni T, Dennis EA. Interfacial properties and critical micelle concentration of lysophospholipids. *Biochemistry*. 1989;28:5113-5120.
55. Ikeda K, Shimizu T, Taguchi R. Targeted analysis of ganglioside and sulfatide molecular species by LC/ESI-MS/MS with theoretically expanded multiple reaction monitoring. *J Lipid Res*. 2008;49:2678-2689.
56. Ju DD, Lai CC, Her GR. Analysis of gangliosides by capillary zone electrophoresis and capillary zone electrophoresis-electrospray mass spectrometry. *J Chromatogr A*. 1997;779:195-203.
57. Couto D, Melo T, Maciel E, et al. New insights on non-enzymatic oxidation of ganglioside GM1 using mass spectrometry. *J Am Soc Mass Spectrom*. 2016;27:1965-1978.
58. Kong J, Yu S. Fourier transform infrared spectroscopic analysis of protein secondary structures. *Acta Biochim Biophys Sin*. 2007;39:549-559.

59. Gu L, Liu C, Stroud JC, Ngo S, Jiang L, Guo Z. Antiparallel triple-strand architecture for prefibrillar Abeta42 oligomers. *J Biol Chem*. 2014;289:27300-27313.
60. Huang D, Zimmerman MI, Martin PK, Nix AJ, Rosenberry TL, Paravastu AK. Antiparallel beta-sheet structure within the C-terminal region of 42-residue Alzheimer's amyloid-beta peptides when they form 150-kDa oligomers. *J Mol Biol*. 2015;427:2319-2328.
61. Cerf E, Sarroukh R, Tamamizu-Kato S, et al. Antiparallel beta-sheet: a signature structure of the oligomeric amyloid beta-peptide. *Biochem J*. 2009;421:415-423.
62. G Creasey R, T Gibson C, H Voelcker N. Characterization of fiber-forming peptides and proteins by means of atomic force microscopy. *Curr Protein Pept Sci*. 2012;13:232-257.
63. Downey MA, Giammona MJ, Lang CA, Buratto SK, Singh A, Bowers MT. Inhibiting and remodeling toxic amyloid-beta oligomer formation using a computationally designed drug molecule that targets Alzheimer's disease. *J Am Soc Mass Spectrom*. 2018;30:85-93.
64. Pountney DL, Lowe R, Quilty M, Vickers JC, Voelcker NH, Gai WP. Annular α-synuclein species from purified multiple system atrophy inclusions. *J Neurochem*. 2004;90:502-512.
65. Andersen NH, Liu Z, Prickett KS. Efforts toward deriving the CD spectrum of a 310 helix in aqueous medium. *FEBS Lett*. 1996;399:47-52.
66. Condello C, Lemmin T, Stohr J, et al. Structural heterogeneity and intersubject variability of Abeta in familial and sporadic Alzheimer's disease. *Proc Natl Acad Sci*. 2018;115:E782-E791.
67. Yanagisawa D, Taguchi H, Yamamoto A, Shirai N, Hirao K, Tooyama I. Curcuminoid binds to amyloid-β 1–42 oligomer and fibril. *J Alzheimers Dis*. 2011;24:33-42.
68. Yang F, Lim GP, Begum AN, et al. Curcumin inhibits formation of amyloid β oligomers and fibrils, binds plaques, and reduces amyloid in vivo. *J Biol Chem*. 2005;280:5892-5901.
69. Qiang W, Yau WM, Lu JX, Collinge J, Tycko R. Structural variation in amyloid-beta fibrils from Alzheimer's disease clinical subtypes. *Nature*. 2017;541:217-221.
70. Xu G, Fromholt SE, Chakrabarty P, et al. Diversity in Aβ deposit morphology and secondary proteome insolubility across models of Alzheimer-type amyloidosis. *Acta Neuropathol Commun*. 2020;8:1-17.
71. Das PK, Dean DN. Aqueous RAFT synthesis of glycopolymers for determination of saccharide structure and concentration effects on amyloid beta aggregation. *Biomacromol*. 2017;18:3359-3366.
72. Watts JC, Condello C, Stöhr J, et al. Serial propagation of distinct strains of Aβ prions from Alzheimer's disease patients. *Proc Natl Acad Sci*. 2014;111:10323-10328.
73. Buyukmihci N, Goehring-Harmon F, Marsh RF. Neural pathogenesis of experimental scrapie after intraocular inoculation of hamsters. *Exp Neurol*. 1983;81:396-406.
74. Kimberlin RH, Walker CA. Pathogenesis of scrapie (strain 263K) in hamsters infected intracerebrally, intraperitoneally or intraocularly. *J Gen Virol*. 1986;67(Pt 2):255-263.
75. Liberski PP, Hainfellner JA, Sikorska B, Budka H. Prion protein (PrP) deposits in the tectum of experimental Gerstmann-Straussler-Scheinker disease following intraocular inoculation. *Folia Neuropathol*. 2012;50:85-88.
76. Rasmussen J, Jucker M, Walker LC. Abeta seeds and prions: how close the fit? *Prion*. 2017;1-11.

SUPPORTING INFORMATION

Additional Supporting Information may be found online in the Supporting Information section.

How to cite this article: Saha J, Dean DN, Dhakal S, et al. Biophysical characteristics of lipid-induced Aβ oligomers correlate to distinctive phenotypes in transgenic mice. *The FASEB Journal*. 2021;35:e21318. https://doi.org/10.1096/fj.202002025RR